Real-time ratiometric optical nanoscale thermometry

Yongliang Chen,[†] Chi Li,[†] Tieshan Yang,[†,‡] Evgeny A. Ekimov, [§, ‖] Carlo Bradac,[#] Son Tung Ha,[††] Milos Toth, [†,‡] Igor Aharonovich[†,‡] and Toan Trong Tran[†,‡‡,*]

[†]School of Mathematical and Physical Sciences and [‡]ARC Centre of Excellence for Transformative Meta-Optical Systems (TMOS) and [‡‡]School of Electrical and Data Engineering University of Technology Sydney, Ultimo, NSW, 2007, Australia

[§]Institute for High Pressure Physics, Russian Academy of Sciences, Troitsk 142190, Russia

[‖]Lebedev Physics Institute, Russian Academy of Sciences, Moscow 117924, Russia

[#]Department of Physics & Astronomy, Trent University, 1600 West Bank Drive, Peterborough, ON, K9L 0G2

[††]Institute of Materials Research and Engineering, A*STAR (Agency for Science, Technology and Research), 2 Fusionopolis Way, #08-03 Innovis, 138634, Singapore, Singapore

*Corresponding author: trongtoan.tran@uts.edu.au

ABSTRACT

All-optical nanothermometry has become a powerful, remote tool for measuring nanoscale temperatures in applications ranging from medicine to nano-optics and solid-state nanodevices. The key features of any candidate nanothermometer are brightness, sensitivity and (signal, spatial and temporal) resolution. Here, we demonstrate a real-time, diamond-based nanothermometry technique with excellent sensitivity (1.8 % K^{-1}) and record-high resolution (5.8×10^4 $K \cdot Hz^{-1/2} \cdot W \cdot cm^{-2}$) based on co-doped nanodiamonds. The distinct performance of our approach stems from two factors. i) Temperature sensors—nanodiamonds co-hosting two Group IV colour centers—engineered to emit spectrally-separated Stokes and Anti-Stokes fluorescence signals under excitation by a single laser source. ii) A parallel detection scheme based on filtering optics and high-sensitivity photon counters for fast readout. We demonstrate the performance of our method by monitoring temporal changes in the local temperature of a microcircuit and a $MoTe_2$ field-effect transistor. Our work advances a powerful, alternative strategy for time-resolved temperature monitoring and mapping of micro-/nano-scale devices

such as microfluidic channels, nanophotonic circuits, and nanoelectronic devices, as well as complex biological environments such as tissues and cells.

KEYWORDS: nanothermometers, Anti-Stokes excitation, ratiometric, germanium-vacancy, silicon-vacancy, nanodiamonds, real-time.

Research in nanoscale optical thermometry has recently gained tremendous momentum owing to its ability to determine, remotely, the temperature of microscopic objects with high sensitivity and high spatial resolution.[1-5] This has made nanothermometry a powerful tool for applications in several areas of research, including medicine,[6] biophotonics,[4] and solid-state nanoelectronics.[7-10] The latter is a prime example of how important nanothermometry has become, for the increasing miniaturization of integrated electronics renders heat dissipation a major problem in micro- and nano-devices. At these scales, heat transport is heavily restricted and ceases to obey Fourier's law[11]—which is instead widely applicable to meso- and macro-scopic systems. Highly-localised, thermal hot spots arise frequently in nanoscale electronic devices and can result in detrimental phenomena such as overheating, loss of performance and catastrophic failure.[12] The ability to monitor temperature at the nanoscale is thus of critical importance for developing high-performance computing devices and energy-efficient electronics. Moreover, nanothermometry has found widespread application in life sciences, as temperature plays a key role in cellular metabolic processes,[13, 14] and is showing potential for the design of target-specific diagnostic and therapeutic strategies, such as hyperthermia and immunotherapy.[6, 15-17]

The key constituent of any nanothermometry approach is the sensor. In optical methods, this is usually a fluorescent nanoprobe that reacts to changes in temperature by variations in its fluorescence characteristics. The variety of available optical nanothermometers is large and includes fluorescent dyes,[1, 2] upconversion nanoparticles,[4, 18] semiconductor quantum dots,[19-21] plasmonic nanoparticles,[22] nanodiamonds[23, 24] and hBN nanoflakes.[25] Among these systems, fluorescent nanodiamonds have emerged as some of the most promising thermosensors owing to a combination of appealing properties. They host bright, photostable color centres that are sensitive to temperature; they are biocompatible, while also able to withstand extreme temperatures and harsh chemical environments.[26-28] In typical diamond-based nanothermometry, temperature changes are detected by measuring corresponding variations in the fluorescence spectral features of the color centers. These include measuring either shifts in

the resonance frequencies of optically detected magnetic resonance (ODMR) spectra,[29] or measuring spectral changes in the zero-phonon line (ZPL) emission wavelength,[30] ZPL linewidth[31] or emission intensity.[32] Approaches based on ODMR frequency shifts of the negatively-charged nitrogen-vacancy (NV⁻) center have achieved some of the highest resolutions (~9 mK Hz$^{-1/2}$) in diamond nanothermometry.[23] However, the method suffers from a series of drawbacks. It requires excitation of the nanosensors with microwave (MW) radiation which may induce heating.[33] Moreover, even extremely small, non–quasi-static magnetic and electric fields can cause shifts in the NV spin resonance,[23, 34] which are indistinguishable from those induced by temperature changes and are thus a source of undesired thermal equivalent noise (TEN), unless decoupling spin-echo techniques are used. Finally, these measurements require relatively high laser excitation powers and are generally slow—though the limits in measurement speed can be partly circumvented with specialized techniques.[35]

Partially due to these drawbacks, all-optical nanothermometry techniques based on the fluorescence of diamond color centers have gained attention. For these, both excitation of the centers and detection of their fluorescence are optical, making them highly versatile and attractive for a variety of real-world realizations, especially in biology and nanoelectronics. However, most of these approaches rely on the monitoring and subsequent analysis of target spectral features (ZPL, linewidth, intensity, etc.), which can lead to limited throughput and/or temperature resolution.

A highly-appealing nanothermometry approach employs the intensity ratio of the Stokes emission and the phonon-mediated Anti-Stokes emission of a group IV color center in diamond.[32, 36] When first demonstrated, this method showed sensitivities higher than those of other all-optical methods, with comparable resolutions. However, it requires the consecutive excitation of the colour center with two separate lasers, at wavelengths above and below the emission wavelength. In addition, as most all-optical approaches, it relies on spectral analysis, which causes the aforementioned limits in throughput and/or resolution. Here, we demonstrate a nanothermometry technique that solves these problems and achieves a 30-fold improvement in resolution relative to power density, over the next best all-optical methods, with a comparable sensitivity.[37, 38] The method is based on measuring the Anti-Stokes/Stokes fluorescence intensity ratio of diamond nanoparticles, albeit with two key differences. First, we remove the need for consecutive excitation with two lasers by using nanodiamonds co-doped with Si and Ge. The nanodiamonds host both silicon-vacancy (SiV) and germanium-vacancy (GeV) centers, which are spectrally separated and are simultaneously excited by a single laser in the Stokes and Anti-Stokes regime, respectively. Second, we perform the readout

3

of the SiV and GeV emission intensities in parallel using two photodetectors rather than a spectrometer. This enables the real-time readout of the fluorescence intensity ratio and completely eliminates the need for spectral analysis. Moreover, these benefits are realised whilst achieving a temperature sensitivity and resolution that outperform all existing all-optical nanothermometry techniques. This is important since these metrics ultimately limit the usefulness and applicability of any high-speed nanothermometry technique. Notably, our results show that the multiplexing ability of diamond to emit at different wavelengths (provided that it simultaneously hosts different colour centers) is intrinsically useful, beyond its mere practical convenience for exploiting specific absorption/scattering windows, e.g., in biological applications. In fact, in combination with a purely physical mechanism—the temperature-dependent phonon spectral density in diamond—it allows performing the direct measurement of a physical quantity (temperature in this case). Our method is therefore highly attractive for fast monitoring of temperature variations at the nanoscale, as we demonstrate here using a microcircuit and a multilayer $MoTe_2$ field-effect transistors (FET).

RESULTS AND DISCUSSION

The two types of color centers were incorporated in nanodiamonds using the high-pressure high-temperature (HPHT) growth technique (c.f. Methods).[39] Briefly, a powder mixture of adamantane ($C_{10}H_{16}$), tetraphenylgermane ($C_{24}H_{20}Ge$) and tetraphenylsilane ($C_{24}H_{20}Si$) were pressed into a pellet and placed inside a titanium capsule. The capsule was then compressed at high temperature (1800–2000 °C) and high pressure (8–9 GPa) inside a reaction chamber, and cooled under high pressure to room temperature. The resulting diamond particles were then dispersed in isopropanol (IPA), drop-casted on a clean silicon substrate and left to dry on a hotplate at 60 °C to completely remove the residual solvent. Two representative scanning electron microscopy (SEM) images showing diamonds of different sizes are displayed in **Supporting Information Figure S1a**. The sizes of these diamond particles ranged from a few micrometres to a few hundred nanometers and can be controlled by adjusting the parameters in the synthesis process. By using Raman spectroscopy, we observed the characteristic narrow diamond peak at ~1332 cm^{-1}, (**Supporting Information Figure S1b)** indicating that the particles were high-quality diamonds.
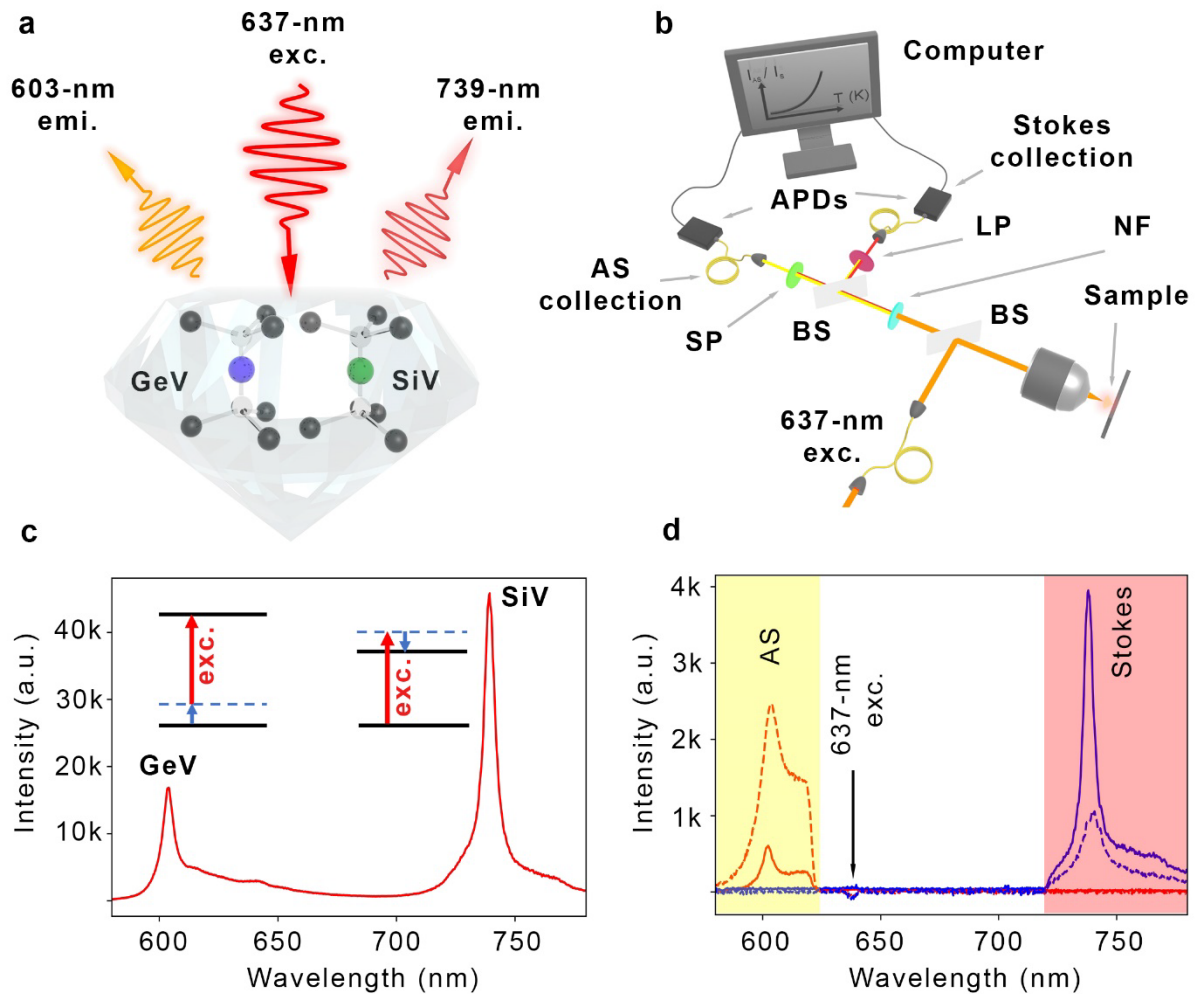
Fig. 1 Anti-Stokes and Stokes photoemission from GeV and SiV centres in a nanodiamond generated by a single excitation source. a, Schematic showing a 637-nm laser (red) used to excite the GeV-SiV co-doped diamonds: Anti-Stokes regime for GeV centers (emitting at 603 nm) and Stokes regime for SiV centers (emitting at 739 nm), respectively. **b**, Schematic of the optical setup. The fluorescence signals from the GeV and SiV centers are split, filtered and collected by two avalanche photodiodes (APDs) on separate arms. BS: beam-splitter; NF: neutral-density filter; LP: long-pass filter; SP: short-pass filter; AS: Anti-Stokes. **c**, Characteristic spectrum showing both the GeV and SiV emission peaks. Here, both centers were excited in the Stokes configuration, using a 532-nm, 300-μW laser. The spot size and power density were 0.93 μm and 40 kW/cm^2, respectively. The inset depicts phonon-absorption and phonon-emission for the excitation of GeV and SiV color centers, respectively. **d**, Two representative spectra obtained with a single 637-nm excitation source at room-temperature (solid lines) and 130 ℃ (dashed lines), displaying both Anti-Stokes (GeV) and Stokes fluorescence (SiV). The spot size and power density were 1.11 μm and 37 kW/cm^2,

respectively. The transparent yellow and red shadings indicate the filtered bands used for temperature sensing. The acquisition times in **c** and **d** are 1 s and 150 s, respectively.

Figure 1a shows the proposed scheme where a 637-nm laser (red arrow) excites the GeV center (Anti-Stokes) and SiV center (Stokes), producing emission at ~603-nm (orange arrow) and ~739-nm (dark red arrow), respectively. The 637-nm wavelength for the excitation laser was chosen because it lies within the phonon sideband (PSB) of GeV centers and had been previously demonstrated to efficiently excite these centers in the Anti-Stokes regime. Any wavelength in the range ~625–670 nm can be used, as in this range both GeV and SiV centers are excited.

To characterize the behavior of the co-doped diamonds, we use a lab-built confocal microscope shown in **Figure 1b** (c.f. Methods). The fluorescence signal from the diamond nanoparticles is split into two collection arms where two separate fiber-coupled avalanche photodiodes (APDs) collect the filtered signal from either the GeV or SiV centers. This allows us to obtain the real-time GeV (Anti-Stokes)/SiV(Stokes) fluorescence intensity ratio which is directly translated into a temperature value using a calibration curve (see below). This eliminates completely the need to collect spectra and to perform post-processing steps conventionally used in analogous methods.

Figure 1c displays the main spectral properties of the engineered nanodiamonds co-doped with GeV and SiV centers. The spectrum in the figure was obtained using a continuous-wave 532-nm excitation laser, at room-temperature, to enable the observation of emission from both centers. Two prominent sharp peaks are clearly visible; they are the characteristic ZPL wavelengths of the GeV (emission at ~603 nm) and the SiV centers (emission at ~739 nm). To verify the feasibility of the proposed nanothermometry technique, we then excited the same nanodiamond with a 637-nm laser, which should excite the GeV and the SiV centers in the Anti-Stokes and Stokes regime, respectively. As shown in the inset of Figure 1c, the excitation of the GeV centers involves the absorption of phonons while the excitation of the SiV centers features the emission of phonons. We conducted the measurement at two different temperatures as shown in **Figure 1d**. At room-temperature, the intensity of the GeV peak (~603 nm) was almost 8 times smaller than that of the SiV peak (~739 nm). At 130 °C, however, the intensity of the GeV peak was nearly 2.5 times higher than that of the SiV peak. Such a drastic change in the intensity ratio of GeV to SiV peak with temperature indicates that the ratio is suitable for high-sensitivity thermometric measurements. The changes in fluorescence of the GeV and SiV

centers are attributed to competing mechanisms. Briefly, an increase in temperature causes a decrease in fluorescence due primarily to the activation of non-radiative decays from the excited state.[40, 41] This behaviour is the main factor determining the temperature response of SiV centers, which are excited in the Stokes regime. While this mechanism is still present for the GeV centers, their fluorescence response to temperature changes is dominated by the temperature dependence of the phonon spectral density, i.e., the phonon density of states multiplied by the transition amplitude—which follows Arrhenius-like scaling. This is because the GeV centers are excited in the Anti-Stokes regime, with a low-energy (long-wavelength) laser. Their optical transition to the first excited electronic state thus depends on them being in an excited vibronic state, populated via the absorption of phonons by ground-state electrons, and depends strongly—in fact, exponentially (see below)—on temperature.[32]
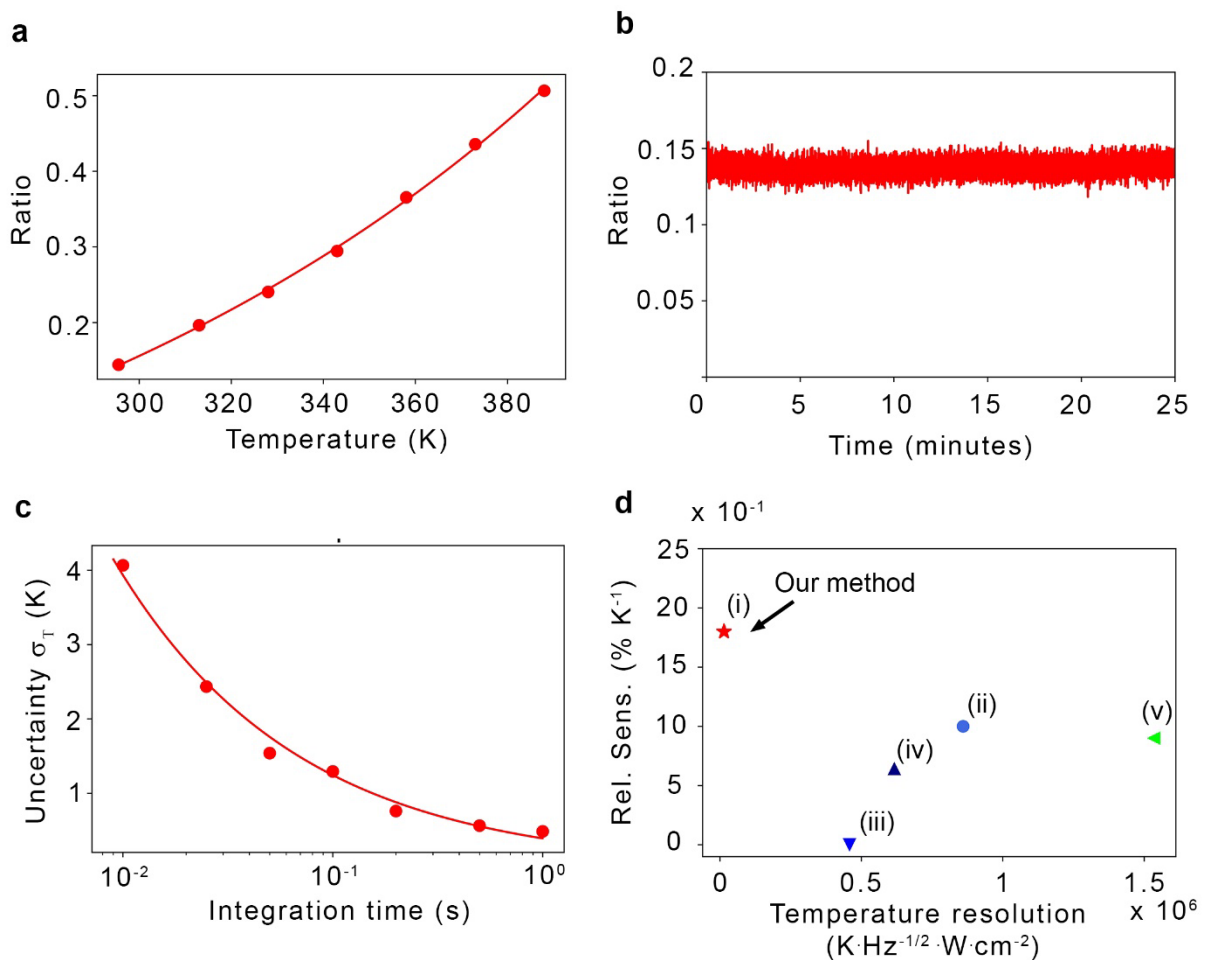

Fig. 2 Nanothermometry based on the GeV/SiV Anti-Stokes/Stokes emission ratio. a, Temperature dependence of the GeV/SiV fluorescence intensity ratio from a nanodiamond, measured by two avalanche photodiodes (APDs). Each data point is calculated by collecting the intensities for 10 s, with 50-ms integration time. The error bars are calculated by taking the

standard deviation of all values measured at every single temperature and are smaller than the size of the markers. The red solid line is an exponential fit. **b**, Long-term time trace of the GeV/SiV fluorescence ratio at room temperature over 25 minutes, showcasing the stability of the measurement. The ratio trace is recorded at 50-ms integration time. **c**, Temperature uncertainty (σ_T) of the thermometer as a function of integration time. The temperature resolution is $\eta_T = \sigma_T \sqrt{t_m}$, where t_m is the integration time, and can be extracted from the shot noise fit (red solid line). Each data point is calculated from a total acquisition of 10 s for different integration times. All the measurements were performed using a 400-μW, 637-nm CW excitation laser. **d**, Relative sensitivity plotted versus temperature resolution for several different systems (the resolution on the x-axis is multiplied by the excitation power density): (i) this technique, (ii) intensity of the ZPL of the NV centers in diamond, (iii) wavelength shift of SiV centers in diamond, (iv) linewidth of GeV centers in diamond, (v) fluorescence peaks ratio of $NaLuF_4$:Yb, Er upconversion nanoparticles. Note that techniques vi–x (see main text) are not shown as the power density information is not available (see also Table 1).

Table 1. Benchmarking of various all-optical nanoscale thermometers on the basis of relative sensitivity, temperature resolution and temperature resolution relative to power density. (i) Our technique, (ii) intensity of the ZPL of diamond NV centers, (iii) wavelength shift of diamond SiV centers, (iv) linewidth of diamond GeV centers, (v) fluorescence peaks ratio of $NaLuF_4$:Yb, Er upconversion nanoparticles, (vi) fluorescence peaks ratio of $(Gd,Yb,Er)_2O_3$ upconversion nanoparticles, (vii) wavelength shift of the emission from CdSe quantum dots, (viii) changes in fluorescence lifetime of CdTe quantum dots, (ix) wavelength shift of the emission from triarylboron organic dyes, (x) fluorescence intensity of rhodamine-B organic dyes. (For techniques vi–x, the power density data is not available).

Group	Thermometers	Rel. Sensitivity (% K^{-1})	Temperature resolution (K·Hz$^{-1/2}$)	Temperature resolution relative to power (K·Hz$^{-1/2}$·W·cm^{-2})

NDs	GeV/SiV (AS/S ratio)	1.8	0.39	1.45×10^4
	NV (ZPL intensity)[24]	1.0	0.30	8.6×10^5
	SiV (wavelength shift)[30]	1.61×10^{-3}	0.36	4.6×10^5
	GeV (linewidth)[31]	0.64	0.30	6.2×10^5
UCNPs	NaLuF$_4$:Yb, Er (PL ratio)[42]	0.9	0.50	1.5×10^6
	(Gd,Yb,Er)$_2$O$_3$ (PL ratio)[43]	1.5	1.00	—
QDs	CdSe (wavelength shift)[19]	1.61×10^{-2}	1.00	—
	CdTe (PL lifetime)[44]	0.8	0.50	—
ODs	Triarylboron (wavelength shift)[45]	0.5	1.00	—
	Rhodamine-B (PL Intensity)[46]	2.0	0.80	—

We now characterize the performance of our ratiometric thermometer. We first established a temperature calibration curve by exciting a representative diamond particle with a 637-nm laser at 400 µW while increasing the temperature from 295.5 to 388 K in steps of 15 K and measuring the corresponding GeV/SiV emission intensity ratio. As the temperature increases, the GeV fluorescence count rate increases, whereas that of the SiV reduces (**Supporting Information Figure S2**). **Figure 2a** shows a plot of GeV/SiV fluorescence ratio as a function of temperature (red circles). As per our prior discussion on the GeV's and SiV's photoluminescence dependence on temperature, the data is well fitted with an exponential function $f(T) = y_0 + a * e^{\left(\frac{-b}{T - T_0}\right)}$, where $f(T)$ is the fitting function, y_0 is the vertical offset, T_0 is the horizontal offset, and a and b are fitting coefficients.[32] From the fit, we obtained a relative sensitivity $S_r = \frac{1}{O} \frac{dO}{dT}$, where O is the measured observable, of 1.8 % K^{-1} at 300 K and 0.011 K^{-1} at 388 K. To examine the consistency of the fluorescence ratio, we recorded such a ratio as a function of temperature over the course of 25 minutes as shown in **Figure 2b**. A small ratio fluctuation

of 4.5×10^{-3} was extracted from the plot, indicating that the variance of the measured observable is small, which translates into a corresponding small error for the measured temperature. Furthermore, we tested the repeatability of the nanothermometer by subjecting it to two heating-cooling cycles and monitoring the fluorescence ratio as shown in **Supporting Information Figure S3**. The negligible differences between the calibration curves indicate that the thermometer is, in fact, very robust. Notably, the fluorescence ratio is robust with various excitation powers and varies only slightly as the excitation power is changed ($3.7 \times 10^{-4}\,\mu W^{-1}$) as illustrated in **Supporting Information Figure S4**.

By varying the integration times of the avalanche photodiodes (APDs) and calculating the standard deviation of the observable, we derived the ratio uncertainty versus integration time. The temperature resolution η_T relates to the temperature uncertainty σ_T and integration time t_m via the relation: $\eta_T = \sigma_T \sqrt{t_m}$. **Figure 2c** shows such relation with a shot noise fit function $\frac{1}{\sqrt{t_m}}$, where t_m is the integration time. The fit was in good agreement with our experimental data, revealing a temperature resolution $\eta_T = 0.39\,K \cdot Hz^{-1/2}$ (at an excitation power of 400 µW). This value is superior to our previous study—where we employed two consecutive (Anti-Stokes and Stokes) excitation cycles to obtain the fluorescence ratio from a single type of color center (GeV) as our temperature observable.[32] Additionally, here we employ a single excitation laser (at 637 nm) to simultaneously excite both the Anti-Stokes (GeV) and Stokes (SiV) emissions. The emissions are acquired in parallel using low-noise, fast APDs which make our current technique superior by any metric, whilst also being simpler.

To benchmark the performance of our nanothermometer against other nanoscale all-optical methods in the literature, we considered the two typical attributes of a thermometer, temperature resolution and relative sensitivity. **Table 1** and **Figure 2d** show a comparison of several representative different systems. Note that **Table 1** has more entries than **Figure 2d**, this is because in **Figure 2d** we plotted on the x-axis the resolution times the power density and the latter is not given in many studies. It is however a crucial parameter as resolution is a relative quantity that increases with signal to noise ratio which is a function of power density as well as integration time. In **Figure 2d**, our method is marked as (i) and the other systems are listed from (ii) to (v). These include techniques based on: (ii) intensity of the ZPL of the NV centers in diamond,[24] (iii) wavelength shift of SiV centers in diamond,[30] (iv) linewidth of GeV centers in diamond,[31] (v) fluorescence peaks ratio of $NaLuF_4$:Yb, Er upconversion nanoparticles.[42] Table 1 additionally includes techniques based on: (vi) fluorescence peaks ratio of $(Gd,Yb,Er)_2O_3$ upconversion nanoparticles,[43] (vii) wavelength shift of the emission

from CdSe quantum dots,[19] (viii) changes in fluorescence lifetime of CdTe quantum dots,[44] (ix) wavelength shift of the emission from triarylboron organic dyes[45] and (x) fluorescence intensity of rhodamine-B organic dyes.[46] Compared to these systems, our nanothermometer fares significantly better, both for temperature resolution relative to power density and for relative sensitivity. With reference to **Figure 2d**, the temperature resolution relative to power density of our technique is 5.8×10^4 K·Hz$^{-1/2}$·W·cm^{-2}, over 30-fold higher than that (1.8×10^6 K·Hz$^{-1/2}$·W·cm^{-2}) of the next best method (iii). Such a metric is especially important for applications involving fragile samples such as biological structures or atomically-thin materials, for which laser excitation with a high-power density may induce optophoresis or damage. Also, a laser excitation greater than a few milliwatts of power might induce heating, due to absorption from diamond impurities and surface carbon, as well as in the case of poor thermal contact between the nanodiamond and its surrounding environment.[47] This is obviously undesired for temperature sensing applications, and it highlights the importance of achieving a target resolution with a relatively lower laser power. The relative sensitivity of our current method is 1.8 % K^{-1}, which is also better by a factor ~2 than that (1.0 % K^{-1}) of the next best method (ii).
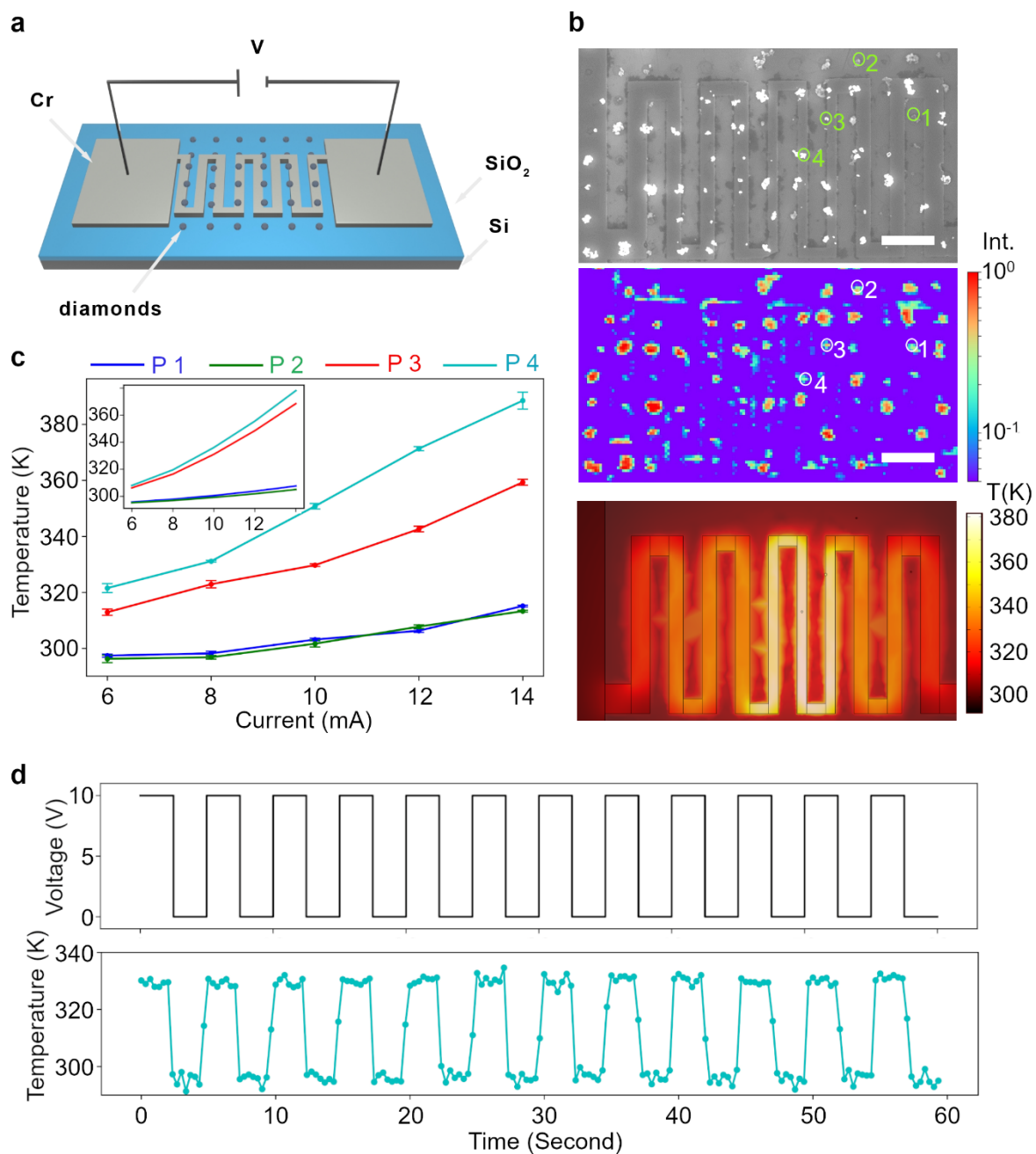
Fig. 3 Real-time temperature monitoring at localized points of a microcircuit. a, Schematic illustration of the microcircuit and the array of diamonds nanothermometers. **b**, SEM image (top panel) and corresponding confocal photoluminescence (PL) map of the microcircuit with a 7×13 array of nanodiamonds (middle panel). The microcircuit was fabricated by electron beam lithography (EBL). The nanodiamond array was produced via capillary assembly of nanodiamonds into an array of 2-μm CSAR (resist) holes patterned by EBL (see main text). A positioning accuracy of ~70% was achieved after removing the polymer resist.[48] The confocal PL map was collected using a 25-μW, 532-nm green CW excitation laser. The inset scale bar

is 10 μm and the color bar of the map is the normalized intensity on a logarithmic scale. Simulated heat distribution of the microcircuit (bottom panel). **c**, Estimated temperature as a function of input current flown into the microcircuit from four representative nanodiamonds whose positions are marked with circles in (b). The temperature readout of each point was calculated from averaging five, 2-s measurements. The error bars were obtained by calculating the standard deviation from the five averaged data points. Each of the 2-s acquisitions was collected at 50-ms APD integration time, under the excitation of 400 μW of a 637-nm CW laser. Inset plot shows the simulated temperature as a function of input current for the four corresponding nanodiamonds. **d**, Top panel: modulated square-wave voltage (0.2 Hz, with a 50 % duty cycle) as a function of time. Bottom panel: corresponding real-time temperature readouts as a function of time acquired from the nanodiamonds in position 4. Each temperature readout was directly extracted from the corresponding fluorescence ratio, with an integration time of 200 ms—corresponding to a temperature uncertainty of 0.76 K.

Such superior performance compared to other nanothermometers stems from two factors: *i*) the Arrhenius-type exponential dependence of the emission ratio with respect to temperature—which is a result of the different dominating mechanisms for the photoluminescence of the GeV (Anti-Stokes) and SiV (Stokes) centers, respectively—and *ii*) the higher doping density of both GeV and SiV color centers compared to a previous study.[32] Finally, we demonstrate the temperature sensing capabilities of our thermometer on actual devices, starting with monitoring real-time temperature of a microcircuit. **Figure 3a** shows a schematic of our serpentine-shaped microcircuit with sections of decreasing width from the extremities to the middle: respectively 6 μm, 4 μm and 2 μm. We patterned the microcircuit using electron-beam lithography (EBL) and deposited a thin layer of chromium (200 nm) to form a complete circuit. At micron-sized widths with a serpentine shape, such a device restricts the electron flow, resulting in the formation of local hotspots—an ideal testbed for demonstrating the performance of our nanothermometer.[49] To enable the deposition of nanodiamonds in a patterned array, we employed a capillary-assembly technique (c.f. Methods).[48] Briefly, we patterned an array of 2-μm holes using the CSAR resist; liquid droplets of a nanodiamonds solution were then slowly dragged across the surface of the substrate, forcing the nanodiamonds into the holes with ~70% yield (**Supporting Information Figure S5**). **Figure 3b** shows wide-field microscopy, SEM, and confocal microscopy images of the area of interest, where an array of nanodiamonds is clearly visible on the circuit. Further improvements on the yield can be made with additional surface functionalization steps for both the nanodiamonds and the open-aperture areas of the

substrate.[50] The array of nanodiamonds allows for pixel-by-pixel thermal mapping of the microcircuit, since all the nanodiamonds are individually calibrated prior to the temperature mapping. The calibration procedure is necessary to eliminate any differences in the temperature response of different nanodiamonds. To demonstrate the working principle of our approach, we chose four representative nanodiamonds at four different locations (marked with circles). We first tested the circuit by collecting its I-V curve (**Supporting Information Figure S6**) which showed the expected linear relationship between input current and voltage (i.e. its Ohmic behavior). Next, we collected individual temperature calibration curves for each selected nanodiamond. The calibration curves were loaded into a script so that, during an actual measurement, the GeV(Anti-Stokes)/SiV(Stokes) intensity ratios could be translated—in real-time—to corresponding temperature values. **Figure 3c** features a plot of predicted temperatures as a function of the input current (6–14 mA) in the microcircuit, based on the four target nanodiamonds. As the nanodiamond in position 4 lied directly above the 2-μm section of the circuit, it exhibited the largest change (68 K) in temperature, increasing from 321 to 389 K. The nanodiamond in position 3 was situated at the edge of the circuit, and thus experienced a smaller temperature increase (46 K) compared to that of the nanodiamond in position 4. The other two nanodiamonds, at position 1 and 2, were ~2–3 μm away from the circuit, and hence showed the smallest temperature difference (17 K).

To verify our experimental results, we conducted a simulation of the thermal distribution on the microcircuit using COMSOL 6.0 Multiphysics ™ (cf. Methods). Figure 3b (bottom panel) shows a simulated heat map from the microcircuit, indicating that the highest temperature is reached in the middle region, where the current flow is restricted the most. As shown in the plot of the temperature as a function of current in the inset of Figure 3c, the experimental results match well the thermal simulation, confirming the temperature readout from the four nanodiamonds.

Next, to demonstrate real-time monitoring of temperature at a particular point of the microcircuit, we chose the nanodiamond at position 4 as a case study since it displays the largest temperature response among the four nanothermometers as shown in figure 3c. By using a signal generator, we modulated the input voltage between 0 and 10 V, in a square-wave pattern at 0.2 Hz and 50% duty cycle, as shown in **Figure 3d**, upper panel. **Figure 3d**, lower panel, shows the corresponding real-time temperature monitoring of the nanodiamond at position 4. It is clear that the temperature switches between 295 and 330 K, as the voltage is accordingly modulated between 0 and 10 V. The fast response indicates that our thermometer is well-suited for nanoscale real-time temperature monitoring.
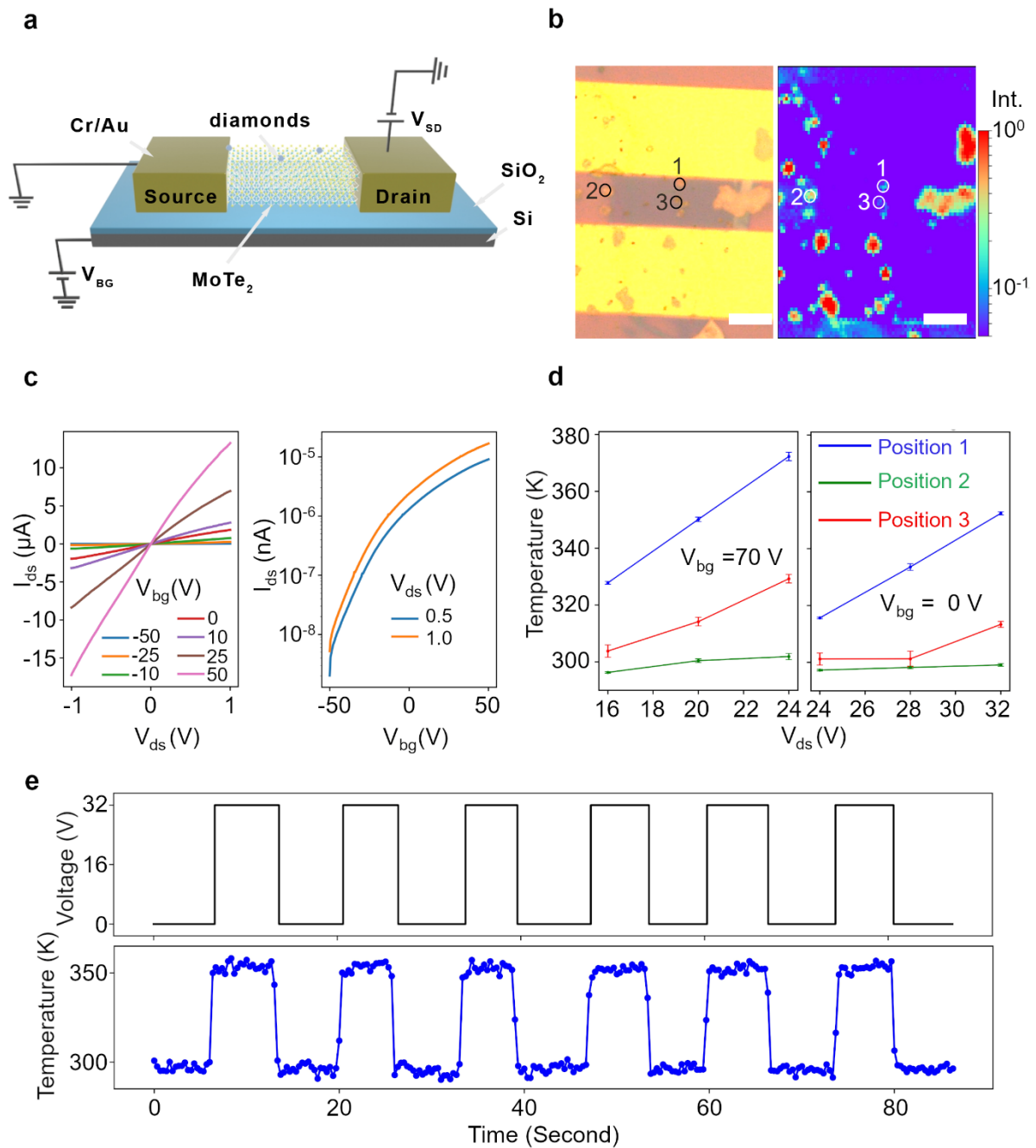
Fig. 4 Real-time temperature monitoring in a MoTe₂ field-effect transistors (FET). a, Schematic illustration of the MoTe₂ FET and of the diamond nanothermometers. **b**, Optical image and corresponding confocal PL map of the device consisting of a pair of Cr/Au (5 nm/80 nm) electrodes deposited on a multilayer MoTe₂ flake. Three representative nanodiamonds at three different locations (black and white circles) chosen for temperature monitoring. The inset scale bar is 5 μm and the color bar of the map is the normalized intensity on a logarithmic scale.

c, Drain-source I-V curves of the MoTe$_2$ FET under different backgate voltages (left panel), and transfer characteristics of the MoTe$_2$ FET under the drain-source voltage of 0.5 V and 1 V, on a logarithmic y-axis scale (right panel). **d**, Temperature readouts plotted versus input drain-source current for the nanodiamonds at three selected locations (shown in (b)), in the MoTe$_2$ FET under a backgate voltage of 70 V (left panel) and 0 V (right panel). Each temperature readout was calculated from five sets of 2-s acquisitions. The integration time was 50 ms under the excitation of 500 μW of a 637-nm CW laser. **e**, Upper panel: modulated square-wave voltage as a function of time. Lower panel: the corresponding real-time temperature readout as a function of time acquired from the nanodiamond in position 1. The applied drain-source voltage was 32 V under the backgate voltage of 0 V. Each temperature readout was calculated from the fluorescence ratio, with an integration time of 200 ms. We also show that one could trade off temperature resolution for integration time and vice versa, as shown in **Supporting Information Figure S7**.

To further test our thermosensor, we performed real-time temperature monitoring on a working field-effect transistor (FET). Specifically, we chose molybdenum ditelluride (MoTe$_2$) as it is a good example of a two-dimensional semiconductor. Such field-effect transistors made from transition metal dichalcogenides (TMDs) have been of intense research interest recently, owing to their potential in the manufacturing of ultra-thin wearables[51, 52] and high-density vertical electronics.[53-55] Heat distribution within these extremely thin devices has, however, remained poorly understood.[56] To fabricate the device, we first exfoliated MoTe$_2$ onto a 300-nm thick SiO$_2$-on-silicon substrate and selected the thin flakes (~5 nm). The electrode patterns in contact with the MoTe$_2$ flake were made using EBL, and thin layers of chromium (5 nm) and gold (80 nm) were deposited to make the drain and source electrodes, as shown in **Supporting Information Figure S8a**. We used Raman spectroscopy to confirm the selected MoTe$_2$ was of high-quality (**Supporting Information Figure S8b**) and employed atomic force microscopy (AFM) to determine the thickness of the flake to be ~5 nm. We then drop-casted the nanodiamonds on the transistor and used them to measure local temperature in real-time. Similar to the measurements in Figure 3, we obtained temperature calibration curves for individual nanodiamonds to ensure accurate temperature readouts from the device. **Figure 4a** shows a simplified schematic of our FET device, where the drain and source electrodes are in good contact with the MoTe$_2$ flake, and the bottom silicon acts as the backgate to exert an out-of-plane electric field on the flake—controlling the current flow across the device. As shown in the optical image and confocal map in **Figure 4b**, there were several nanodiamonds in the

region of interest of the device. We selected three representative nanodiamonds at position 1, 2, and 3 to monitor the local temperature of the device. To ensure that the device behaved as a field effect transistor, we first obtained the drain-source I_{ds}-V_{ds} curves at different backgate voltages, V_{bg}, as shown in **Figure 4c**, left panel. The larger V_{bg} resulted in a steeper I_{ds}-V_{ds} slopes—in good agreement with previous works.[57, 58] We also tested the transfer characteristics of the transistor at 0.5 and 1 V of the drain-source voltage V_{ds} (**Figure 4c**, right panel) and found that such behaviors were in accordance with earlier reports on this type of transistor.[57, 58]

We now turn to the temperature monitoring of the transistor using the nanodiamonds. **Figure 4d** shows two plots of local temperature as a function of V_{ds} , with two different V_{bg} at 70 V and 0 V, for the three nanodiamonds. We first examined the plot with $V_{bg} = 70$ V (left panel). The diamond at position 1, situated at the boundary of the electrode and the MoTe$_2$, exhibited the largest increase in temperature, 44 K, from 328 to 372 K, when V_{ds} changed from 16 to 24 V. Such a large temperature increase can be attributed to the Schottky barrier at the metal-semiconductor junction, resulting in massive heat accumulation in this area. A similar result was reported in an analogous study, showing a temperature increase of ~80 K over a distance of 2μm.[59] The nanodiamond located at position 3 experienced significantly less heating, with only a 25 K increase in temperature under the same conditions. The nanodiamond at position 2 experienced a relatively modest increase in temperature, 6 K, consistent with its location at the boundary between the MoTe$_2$ flake and the substrate. With $V_{bg} = 0$ V (right panel), a similar trend was observed for the three nanodiamonds, allowing us to extract information about the local heat distribution pattern on the transistor, while in operation. Finally, to monitor the real-time temperature of the device at position 1, we generated a modulated signal of V_{ds} between 0 and 32 V with the fixed V_{bg} at 0 V (**Figure 4e**, top panel), and recorded the temperature of the nanodiamond as a function of time. As shown in **Figure 4e**, bottom panel, the changes in temperature were in accordance with that of the voltage modulation, showing a 56 K difference in temperature between 0 and 32 V of V_{ds}. It should be noted that our technique employs a much lower excitation power than other nanothermometry methods. This is relevant as optical illumination can cause photoinduced damage of fragile samples such as 2D materials (e.g., the MoTe$_2$ monolayers used in this study), as shown in Supporting Information Figure S9.

CONCLUSIONS

To conclude, we demonstrated a real-time nanothermometry approach that utilizes the fluorescence intensity ratio between GeV (Anti-Stokes regime) and SiV (Stokes regime) in nanodiamonds engineered to be co-doped with both centers. Whilst in this work we show the approach for the pair of GeV and SiV color centers in diamond, its applicability extends to pairs of optically active defect centers or fluorophores in other suitable materials. These include, but are not limited to, other wide-bandgap semiconductors and insulators, provided that the excitation wavelength is simultaneously located at the emission phonon sideband of one emitter and the absorption phonon sideband of the other. We also show that the nanothermometer has excellent sensitivity (1.8 % K^{-1} at 300 K) and temperature resolution relative to power density (5.8×10^4 K·Hz$^{-1/2}$·W·cm^{-2}). These are comparable to and ~30× better, respectively, than those of the next best all-optical nanothermometers. It should be noted that temperature resolution can be further improved, for instance, by increasing the density of emitters or exploiting multi-variable analysis.[60] We demonstrated the suitability of our nanothermometer for fast, real-time monitoring of local temperature in a microcircuit and a MoTe$_2$ field-effect transistor. When combined with the deterministic deposition of arrays of nanodiamonds, pixel-by-pixel thermal mapping can be achieved in these devices. Our work introduces a fast temperature monitoring and mapping technique for micro- and nano-scale devices such as nanoelectronic circuits, microfluidic channels and nanophotonic devices, as well as of complex biological environments like tissues and cells.

METHODS

Sample preparation

Ge- and Si- co-doped nano-/micro-diamonds were produced at high pressures and temperatures in C-H-Si(0.19 at%)-Ge(0.2 at%) growth system. Micro-diamonds were synthesized at a pressure of 8 GPa and a temperature of 1800–2000 °C, while nanodiamonds at higher pressure of 9 GPa and reduced temperature of 1500–1600 °C for about 60 s. For the synthesis experiments, powder mixture of Adamantane C$_{10}$H$_{16}$ (300 mg, > 99%, Sigma-Aldrich), Tetraphenylgermane C$_{24}$H$_{20}$Ge (15mg, 96%, Aldrich) and Tetraphenylsilane C$_{24}$H$_{20}$Si (18mg, 96%, Aldrich) were mixed in a mortar and pestle, both made of jasper, for about 5 min, pressed into a pellet (65 mg) and placed inside a titanium capsule (6 mm in diameter, 4 mm in height, with 0.2-mm wall thickness). A toroid-type, high-pressure chamber was used to generate pressure and temperature in the reaction cell.[39] After the treatment, samples were quenched under pressure to room temperature.

The nanodiamonds were then dispersed in isopropanol (IPA) at the concentration of 0.1% (w/w). The size of the nanodiamonds were ~300-500 nm. Five microliters of the solution were drop-cast on a clean 0.5 x 0.5 cm^2 silicon substrate and left to dry on a hotplate at 60 ℃ to completely remove the residual solvent. The silicon chip was then ready to be used for optical or structural characterization. The concentration of silicon and germanium vacancy centres obtained by the synthesis process employed in this study is estimated to be ~ppb.[61]

Device fabrication

Preparation of Microcircuits. A volume of ~0.1 mL of polymethyl methacrylate resist solution (950 PMMA) was spun-cast on the thermally-grown SiO$_2$ (~300 nm) on Si substrate for 1 min at 3000 rpm to get a resist coating with the thickness of ~200 nm. The resist coating was then patterned using a scanning electron microscopy (SEM) (Zeiss Supra 55VP) coupled to the Raith electron beam lithography (EBL) system. The resist pattern was subsequently formed by immersing in the resist developer (a methyl isobutyl ketone (MIBK)/isopropyl alcohol (IPA) (1:3) solution) for 30 seconds and the resist stopper (IPA) for 1 min. After cleaning the resist residual of the pattern area via O$_2$ plasma for 10 s under 50 sccm O$_2$ and 100 W power, 200 nm of chromium was deposited onto the patterned resist coating using a lab-built plasma-assisted sputter deposition chamber. The microcircuit was obtained by immersing into the resist remover (99%, acetone) to eliminate the remaining resist and excessive metal.

Preparation of MoTe$_2$ transistor. MoTe$_2$ flakes were mechanically exfoliated from bulk MoTe$_2$ crystal onto a silicon substrate with a 285-nm thermally grown silicon dioxide layer using the scotch tape method.[62] A few-layer MoTe$_2$ flake (<10 nm) was selected based on its optical contrast and its thickness was measured using an atomic force microscopy (AFM, Park XE7). A 2-hour, 200 ℃ annealing process under 50 sccm Ar was adopted to remove the excessive contamination of the flake source and increase the interaction force between the substrate and the flake. Furthermore, two electrode contacts (source and drain) aligned with the targeted flake were formed via electron beam lithography. First, a 300-nm positive e-beam resist (CSAR 13.5%) was coated to the substrate at a spin rate of 4000 rpm for 1 minute, followed by 170 ℃ baking on a hotplate to remove the residual solvent. For aligning the pattern and targeted MoTe$_2$ flake, focused electron beams (20 keV) at very low beam current (37 pA) were used to avoid exposure of the unpatterned area. Then the pattern structures were irradiated at a dosage of 150 μC/cm^2. The source-drain channel width is 6 μm. After a development process, 5 nm of chromium and 80 nm of gold were deposited by thermal evaporation deposition. The remaining metals were removed in the lift-off process. Ten microliters of

nanodiamonds solution were drop-cast onto the substrate to deposit a few nanodiamonds on the transistor and let it dry naturally in air.

Preparation of an array of nanodiamonds on microcircuit. To deposit diamond particles on the microcircuit, a second EBL patterning step was performed to create an array of open apertures. Ten microliters of nanodiamonds aqueous solution (0.5% w/w) containing 0.01% CTAB (Hexadecyltrimethylammonium bromide) surfactant were drop-casted on the substrate and a thin coverslip was slowly glided at an angle across the substrate to assist the insertion of the nanodiamonds into the apertures. The substrate was then dried naturally in air. The details of the process can be found elsewhere.[48]

Optical characterization

Optical characterization of the quantum emitters was conducted using a lab-built confocal microscope. The sample was glued using silver paste onto the high-precision temperature-controlled stage (Microptik, MHCS-622) with a temperature resolution of 0.1 K. A 637-nm continuous wave (CW) laser beam was focused onto the diamond particles through a long-working-distance objective with a numerical aperture of 0.7 (Mitutoyo, Plan Apochromat, 100×). The laser spot size (the airy disk diameter) is calculated to be $D = \frac{1.22*\lambda}{NA} = 1.11\ \mu m$. A typical excitation power of 400 µW was used to ensure that laser-induced heating was negligible in our experiments. Specifically, we observed heating due to laser excitation (determined from monitoring broadening of the emission linewidths) only for excitation power above 2 mW. A fast-steering mirror (Newport, FSM-300-01) was used to control the laser spot position and scan across the sample to generate a confocal map. The excitation laser and the photoluminescence (PL) signals were separated by a plate beam splitter (70T:30R) (Thorlabs). The collection arm was further split into two paths, one for the GeV emission (anti-Stokes PL) and the other for the SiV emission (Stokes PL). To completely suppress the 637-nm excitation laser, we inserted a single notch filter (Semrock, NF03-642E-25) in the main collection arm, as well as a tuneable shortpass filter (Semrock, TSP01-628-25x36) for the GeV collection path and a tunable longpass filter (Semrock, FF01-715/LP-25) for the SiV counterpart. The tuneable spectral filters allow for the selection of two collection bands, as shown in Figure 1d. Specifically, the filters were tuned (by mechanical tilting) to set these collection bands for the GeV and SiV emission at 575–625 nm and 720–780 nm, respectively. The choice of these filters/spectral bands was made to maximize both collection of the two centers'

photoluminescence and suppression of the excitation laser. Each collection arm was fiber-coupled into a graded-index multimode fiber (Thorlabs, GIF625) connected to a single-photon avalanche photodiode (SPAPD) (Excelitas Technologies, SPCM-AQRH-TR) that counts all the incoming photons. A software was developed (LabView) to control all the hardware, analyze the photon rates, take the direct ratio of the GeV to SiV emission intensity, and output the real-time fluorescence ratio based on the individual signals collected at each SPAPD. The typical integration times of the SPAPD in our measurements is 200 ms (or 5 Hz sampling rate). A shorter integration time can be used at the expense of resolution of the measured temperature. Once the temperature calibration curve for a nanothermometer has been determined, as shown in **Figure 2a**, unknown temperatures can be obtained by mapping the ratios directly onto the calibration curve, and they are displayed directly on the software user interface. Alternatively, the photoluminescence from individual nanodiamonds was spectrally analyzed with a spectrometer (Princeton, Acton Series SP2300 series) equipped with a charge-coupled device (CCD) camera (PIXIS series). In most of the optical measurements, the 637-nm laser was pumped at 400 µW of power, measured at the back aperture of the objective. To acquire the full spectra of both GeV and SiV emission, we employed a 532-nm laser with 50 µW of power.

To estimate σ_T, we apply the standard deviation of all the corresponding temperature values during one 10 s time trace of emission ratios for various APD integration times. Each temperature value is estimated by mapping each emission ratio onto the temperature calibration curve shown in Figure 2a. The value of σ_T obtained with this procedure is then employed to determine the resolution, η_T, of the nanothermometry technique.

Heat distribution simulation

We simulated the Joule heating effect of the microheater using COMSOL 6.0 Multiphysics™. The temperature of the surrounding air and the silicon substrate were set to be ~ 293.1 K. All material parameters were taken from the COMSOL library and literature, except the electrical conductivity of Chromium components was set to be ~ 3.9×10 S/m instead of ~7.9×10^6 S/m of chromium metal. Such modification is established to correctly represent the electrical conductivity of the sputtered Cr film without post-annealing in the experiments.

ASSOCIATED CONTENT

Data Availability Statement

The datasets generated during and/or analysed during the current study are available from the corresponding author on reasonable request.

Supporting Information

The Supporting Information is available free of charge at https://pubs.acs.org

Characterization of co-doped GeV and SiV nano-/micro-diamonds; avalanche photodiode count rates acquired from the GeV and SiV color centers; repeatability of fluorescence ratio vs temperature; Anti-Stokes (GeV) to Stokes (SiV) fluorescence ratio as a function of excitation power; preparation of an array of nanodiamonds; I-V curve of the microcircuit used in this work; comparison of real-time monitoring at different integration times; optical image of the $MoTe_2$ transistor; demonstration of photoluminescence quenching induced by exposure to a relatively high-power laser.

Preprint

An early version of the current manuscript was submitted at https://arxiv.org/ and can be found in the URL below. Most notably, compared to the preprint version, the current manuscript has been added with heat distribution simulation data using COMSOL 6.0 Multiphysics™ conducted by new author Ha, S. T., whose name has been included in the current version of the manuscript. The current version has also been added with more optical characterization and modified text for improved clarity.

Chen, Y.; Li, C.; Yang, T.; Ekimov, E. A.; Bradac, C.; Toth, M.; Aharonovich, I.; Tran, T. T. Real-time Ratiometric Optical Nanoscale Thermometry. 2021, arXiv:2112.01758. arXiv Preprint. https://arxiv.org/abs/2112.01758v1 (accessed on January 13th, 2023)

AUTHOR INFORMATION

Author contribution

Y. C. and T. T. T conceived the idea of the project. Y.C. and T. T. T built the optical system and its software. E. E. fabricated the co-doped nanodiamonds. Y. C. made the microcircuit, performed the optical characterization and the thermometric measurements. S. T. H. conducted the heat simulation for the microcircuit. C. L., T. Y. and Y. C. fabricated the transistor. Y.C.

and T. T. T analyzed the data. T. T. T supervised the project. All authors discussed the results and commented on the manuscript.

Acknowledgement

Funding Sources

Notes

References

(1) Jaque, D.; Vetrone, F., Luminescence nanothermometry. *Nanoscale* **2012,** *4* (15), 4301-4326.
(2) Brites, C. D. S.; Lima, P. P.; Silva, N. J. O.; Millán, A.; Amaral, V. S.; Palacio, F.; Carlos, L. D., Thermometry at the Nanoscale. *Nanoscale* **2012,** *4* (16), 4799-4829.
(3) Sotoma, S.; Epperla, C. P.; Chang, H.-C., Diamond Nanothermometry. *ChemNanoMat* **2018,** *4* (1), 15-27.
(4) Zhou, J.; del Rosal, B.; Jaque, D.; Uchiyama, S.; Jin, D., Advances and challenges for fluorescence nanothermometry. *Nat. Meth.* **2020,** *17* (10), 967-980.

(5) Bradac, C.; Lim, S. F.; Chang, H.-C.; Aharonovich, I., Optical Nanoscale Thermometry: From Fundamental Mechanisms to Emerging Practical Applications. *Adv. Opt. Mater.* **2020,** *8* (15), 2000183.

(6) Schroeder, A.; Heller, D. A.; Winslow, M. M.; Dahlman, J. E.; Pratt, G. W.; Langer, R.; Jacks, T.; Anderson, D. G., Treating metastatic cancer with nanotechnology. *Nat. Rev. Cancer* **2012,** *12* (1), 39-50.

(7) Yue, Y.; Wang, X., Nanoscale thermal probing. *Nano Rev.* **2012,** *3* (1), 11586.

(8) Schelling, P. K.; Shi, L.; Goodson, K. E., Managing heat for electronics. *Mater. Today* **2005,** *8* (6), 30-35.

(9) Cahill, D. G.; Ford, W. K.; Goodson, K. E.; Mahan, G. D.; Majumdar, A.; Maris, H. J.; Merlin, R.; Phillpot, S. R., Nanoscale thermal transport. *J. Appl. Phys.* **2003,** *93* (2), 793-818.

(10) Cahill, D. G.; Braun, P. V.; Chen, G.; Clarke, D. R.; Fan, S.; Goodson, K. E.; Keblinski, P.; King, W. P.; Mahan, G. D.; Majumdar, A.; Maris, H. J.; Phillpot, S. R.; Pop, E.; Shi, L., Nanoscale thermal transport. II. 2003–2012. *Appl. Phys. Rev.* **2014,** *1* (1), 011305.

(11) Ziabari, A.; Torres, P.; Vermeersch, B.; Xuan, Y.; Cartoixà, X.; Torelló, A.; Bahk, J.-H.; Koh, Y. R.; Parsa, M.; Ye, P. D.; Alvarez, F. X.; Shakouri, A., Full-field thermal imaging of quasiballistic crosstalk reduction in nanoscale devices. *Nat. Commun.* **2018,** *9* (1), 255.

(12) Altet, J.; Claeys, W.; Dilhaire, S.; Rubio, A., Dynamic Surface Temperature Measurements in ICs. *Proceedings of the IEEE* **2006,** *94* (8), 1519-1533.

(13) Tsuji, T.; Ikado, K.; Koizumi, H.; Uchiyama, S.; Kajimoto, K., Difference in intracellular temperature rise between matured and precursor brown adipocytes in response to uncoupler and β-adrenergic agonist stimuli. *Sci. Rep.* **2017,** *7* (1), 12889.

(14) Tsai, P.-C.; Epperla, C. P.; Huang, J.-S.; Chen, O. Y.; Wu, C.-C.; Chang, H.-C., Measuring Nanoscale Thermostability of Cell Membranes with Single Gold–Diamond Nanohybrids. *Angew. Chem. Int. Ed.* **2017,** *56* (11), 3025-3030.

(15) O'Neal, D. P.; Hirsch, L. R.; Halas, N. J.; Payne, J. D.; West, J. L., Photo-thermal tumor ablation in mice using near infrared-absorbing nanoparticles. *Cancer Lett.* **2004,** *209* (2), 171-176.

(16) Zhang, J. Z., Biomedical Applications of Shape-Controlled Plasmonic Nanostructures: A Case Study of Hollow Gold Nanospheres for Photothermal Ablation Therapy of Cancer. *J. Phys. Chem. Lett* **2010,** *1* (4), 686-695.

(17) Moy, A. J.; Tunnell, J. W., Combinatorial immunotherapy and nanoparticle mediated hyperthermia. *Adv. Drug Delivery Rev.* **2017,** *114*, 175-183.

(18) Fischer, L. H.; Harms, G. S.; Wolfbeis, O. S., Upconverting Nanoparticles for Nanoscale Thermometry. *Angew. Chem. Int. Ed.* **2011,** *50* (20), 4546-4551.

(19) Li, S.; Zhang, K.; Yang, J.-M.; Lin, L.; Yang, H., Single Quantum Dots as Local Temperature Markers. *Nano Lett.* **2007,** *7* (10), 3102-3105.

(20) Maestro, L. M.; Rodriguez, E. M.; Rodriguez, F. S.; la Cruz, M. C.; Juarranz, A.; Naccache, R.; Vetrone, F.; Jaque, D.; Capobianco, J. A.; Sole, J. G., CdSe quantum dots for two-photon fluorescence thermal imaging. *Nano Lett.* **2010,** *10* (12), 5109-15.

(21) Maestro, L. M.; Jacinto, C.; Silva, U. R.; Vetrone, F.; Capobianco, J. A.; Jaque, D.; Solé, J. G., CdTe Quantum Dots as Nanothermometers: Towards Highly Sensitive Thermal Imaging. *Small* **2011,** *7* (13), 1774-1778.

(22) Lan, Y.; Wang, H.; Chen, X.; Wang, D.; Chen, G.; Ren, Z., Nanothermometer Using Single Crystal Silver Nanospheres. *Adv. Mater.* **2009,** *21* (47), 4839-4844.

(23) Kucsko, G.; Maurer, P. C.; Yao, N. Y.; Kubo, M.; Noh, H. J.; Lo, P. K.; Park, H.; Lukin, M. D., Nanometre-scale thermometry in a living cell. *Nature* **2013,** *500*, 54.

(24) Plakhotnik, T.; Aman, H.; Chang, H.-C., All-optical single-nanoparticle ratiometric thermometry with a noise floor of 0.3 K Hz−1/2. *Nanotechnology* **2015,** *26* (24), 245501.

(25) Chen, Y.; Tran, T. N.; Duong, N. M. H.; Li, C.; Toth, M.; Bradac, C.; Aharonovich, I.; Solntsev, A.; Tran, T. T., Optical Thermometry with Quantum Emitters in Hexagonal Boron Nitride. *ACS Appl. Mater. Interfaces* **2020,** *12* (22), 25464-25470.

(26) Toyli, D.; Christle, D.; Alkauskas, A.; Buckley, B.; Van de Walle, C.; Awschalom, D., Measurement and control of single nitrogen-vacancy center spins above 600 K. *Physical Review X* **2012,** *2* (3), 031001.

(27) Aharonovich, I.; Englund, D.; Toth, M., Solid-state single-photon emitters. *Nat. Photonics* **2016,** *10* (10), 631-641.

(28) Neumann, P.; Jakobi, I.; Dolde, F.; Burk, C.; Reuter, R.; Waldherr, G.; Honert, J.; Wolf, T.; Brunner, A.; Shim, J. H.; Suter, D.; Sumiya, H.; Isoya, J.; Wrachtrup, J., High-Precision Nanoscale Temperature Sensing Using Single Defects in Diamond. *Nano Lett.* **2013,** *13* (6), 2738-2742.

(29) Wu, Y.; Alam, M. N. A.; Balasubramanian, P.; Ermakova, A.; Fischer, S.; Barth, H.; Wagner, M.; Raabe, M.; Jelezko, F.; Weil, T., Nanodiamond Theranostic for Light-Controlled Intracellular Heating and Nanoscale Temperature Sensing. *Nano Lett.* **2021,** *21* (9), 3780-3788.

(30) Nguyen, C. T.; Evans, R. E.; Sipahigil, A.; Bhaskar, M. K.; Sukachev, D. D.; Agafonov, V. N.; Davydov, V. A.; Kulikova, L. F.; Jelezko, F.; Lukin, M. D., All-optical nanoscale thermometry with silicon-vacancy centers in diamond. *Appl. Phys. Lett.* **2018,** *112* (20), 203102.

(31) Fan, J.-W.; Cojocaru, I.; Becker, J.; Fedotov, I. V.; Alkahtani, M. H. A.; Alajlan, A.; Blakley, S.; Rezaee, M.; Lyamkina, A.; Palyanov, Y. N.; Borzdov, Y. M.; Yang, Y.-P.; Zheltikov, A.; Hemmer, P.; Akimov, A. V., Germanium-Vacancy Color Center in Diamond as a Temperature Sensor. *ACS Photonics* **2018,** *5* (3), 765-770.

(32) Tran, T. T.; Regan, B.; Ekimov, E. A.; Mu, Z.; Zhou, Y.; Gao, W.-b.; Narang, P.; Solntsev, A. S.; Toth, M.; Aharonovich, I.; Bradac, C., Anti-Stokes excitation of solid-state quantum emitters for nanoscale thermometry. *Sci. Adv.* **2019,** *5* (5), eaav9180.

(33) Wang, Z.; Zhang, J.; Feng, X.; Xing, L., Microwave Heating Effect on Diamond Samples of Nitrogen-Vacancy Centers. *ACS Omega* **2022,** *7* (35), 31538-31543.

(34) Fujiwara, M.; Shikano, Y., Diamond quantum thermometry: from foundations to applications. *Nanotechnology* **2021,** *32* (48), 482002.

(35) Tzeng, Y.-K.; Tsai, P.-C.; Liu, H.-Y.; Chen, O. Y.; Hsu, H.; Yee, F.-G.; Chang, M.-S.; Chang, H.-C., Time-Resolved Luminescence Nanothermometry with Nitrogen-Vacancy Centers in Nanodiamonds. *Nano Lett.* **2015,** *15* (6), 3945-3952.

(36) Bradac, C.; Gao, W.; Forneris, J.; Trusheim, M. E.; Aharonovich, I., Quantum nanophotonics with group IV defects in diamond. *Nat. Commun.* **2019,** *10* (1), 5625.

(37) Ansari, A. A.; Sillanpää, M., Advancement in upconversion nanoparticles based NIR-driven photocatalysts. *Renewable and Sustainable Energy Reviews* **2021,** *151*, 111631.

(38) Nexha, A.; Carvajal, J. J.; Pujol, M. C.; Díaz, F.; Aguiló, M., Lanthanide doped luminescence nanothermometers in the biological windows: strategies and applications. *Nanoscale* **2021,** *13* (17), 7913-7987.

(39) Kondrina, K. M.; Kudryavtsev, O. S.; Vlasov, I. I.; Khmelnitskiy, R. A.; Ekimov, E. A., High-pressure synthesis of microdiamonds from polyethylene terephthalate. *Diamond Relat. Mater.* **2018,** *83*, 190-195.

(40) Jahnke, K. D.; Sipahigil, A.; Binder, J. M.; Doherty, M. W.; Metsch, M.; Rogers, L. J.; Manson, N. B.; Lukin, M. D.; Jelezko, F., Electron–phonon processes of the silicon-vacancy centre in diamond. *New J. Phys.* **2015,** *17* (4), 043011.

(41) Neu, E.; Hepp, C.; Hauschild, M.; Gsell, S.; Fischer, M.; Sternschulte, H.; Steinmüller-Nethl, D.; Schreck, M.; Becher, C., Low-temperature investigations of single silicon vacancy colour centres in diamond. *New J. Phys.* **2013,** *15* (4), 043005.

(42) Zhu, X.; Feng, W.; Chang, J.; Tan, Y.-W.; Li, J.; Chen, M.; Sun, Y.; Li, F., Temperature-feedback upconversion nanocomposite for accurate photothermal therapy at facile temperature. *Nat. Commun.* **2016,** *7* (1), 10437.

(43) Debasu, M. L.; Ananias, D.; Pastoriza-Santos, I.; Liz-Marzán, L. M.; Rocha, J.; Carlos, L. D., Nanothermometry: All-In-One Optical Heater-Thermometer Nanoplatform Operative From 300 to 2000 K Based on Er3+ Emission and Blackbody Radiation (Adv. Mater. 35/2013). *Adv. Mater.* **2013,** *25* (35), 4817-4817.

(44) Haro-González, P.; Martínez-Maestro, L.; Martín, I. R.; García-Solé, J.; Jaque, D., High-Sensitivity Fluorescence Lifetime Thermal Sensing Based on CdTe Quantum Dots. *Small* **2012,** *8* (17), 2652-2658.

(45) Feng, J.; Tian, K.; Hu, D.; Wang, S.; Li, S.; Zeng, Y.; Li, Y.; Yang, G., A Triarylboron-Based Fluorescent Thermometer: Sensitive Over a Wide Temperature Range. *Angew. Chem. Int. Ed.* **2011,** *50* (35), 8072-8076.

(46) Ross, D.; Gaitan, M.; Locascio, L. E., Temperature Measurement in Microfluidic Systems Using a Temperature-Dependent Fluorescent Dye. *Anal. Chem.* **2001,** *73* (17), 4117-4123.

(47) Rahman, A. T. M. A.; Frangeskou, A. C.; Kim, M. S.; Bose, S.; Morley, G. W.; Barker, P. F., Burning and graphitization of optically levitated nanodiamonds in vacuum. *Sci. Rep.* **2016,** *6* (1), 21633.

(48) Preuß, J. A.; Rudi, E.; Kern, J.; Schmidt, R.; Bratschitsch, R.; Michaelis de Vasconcellos, S., Assembly of large hBN nanocrystal arrays for quantum light emission. *2D Materials* **2021,** *8* (3), 035005.

(49) Mecklenburg, M.; Hubbard, W. A.; White, E. R.; Dhall, R.; Cronin, S. B.; Aloni, S.; Regan, B. C., Nanoscale temperature mapping in operating microelectronic devices. *Science* **2015,** *347* (6222), 629-632.

(50) Andrich, P.; Li, J.; Liu, X.; Heremans, F. J.; Nealey, P. F.; Awschalom, D. D., Microscale-Resolution Thermal Mapping Using a Flexible Platform of Patterned Quantum Sensors. *Nano Lett.* **2018,** *18* (8), 4684-4690.

(51) Akinwande, D.; Petrone, N.; Hone, J., Two-dimensional flexible nanoelectronics. *Nat. Commun.* **2014,** *5* (1), 5678.

(52) Xu, M.; Liang, T.; Shi, M.; Chen, H., Graphene-Like Two-Dimensional Materials. *Chem. Rev.* **2013,** *113* (5), 3766-3798.

(53) Geim, A. K.; Grigorieva, I. V., Van der Waals heterostructures. *Nature* **2013,** *499* (7459), 419-425.

(54) Fiori, G.; Bonaccorso, F.; Iannaccone, G.; Palacios, T.; Neumaier, D.; Seabaugh, A.; Banerjee, S. K.; Colombo, L., Electronics based on two-dimensional materials. *Nat. Nanotechnol.* **2014,** *9* (10), 768-779.

(55) Wang, Q. H.; Kalantar-Zadeh, K.; Kis, A.; Coleman, J. N.; Strano, M. S., Electronics and optoelectronics of two-dimensional transition metal dichalcogenides. *Nat. Nanotechnol.* **2012,** *7* (11), 699-712.

(56) Yalon, E.; McClellan, C. J.; Smithe, K. K. H.; Muñoz Rojo, M.; Xu, R. L.; Suryavanshi, S. V.; Gabourie, A. J.; Neumann, C. M.; Xiong, F.; Farimani, A. B.; Pop, E., Energy Dissipation in Monolayer MoS2 Electronics. *Nano Lett.* **2017,** *17* (6), 3429-3433.

(57) Yang, Y.; Zhu, X.; Zhang, K.; Zhu, H.; Chen, L.; Sun, Q., Observation of different transport behaviors in a two-dimensional MoTe2 field-effect transistor with engineered gate stack. *Microelectron. Eng.* **2021,** *237*.

(58) Lin, Y. F.; Xu, Y.; Wang, S. T.; Li, S. L.; Yamamoto, M.; Aparecido-Ferreira, A.; Li, W.; Sun, H.; Nakaharai, S.; Jian, W. B.; Ueno, K.; Tsukagoshi, K., Ambipolar MoTe2 transistors and their applications in logic circuits. *Adv. Mater.* **2014,** *26* (20), 3263-9.

(59) Yalon, E.; McClellan, C. J.; Smithe, K. K. H.; Munoz Rojo, M.; Xu, R. L.; Suryavanshi, S. V.; Gabourie, A. J.; Neumann, C. M.; Xiong, F.; Farimani, A. B.; Pop, E., Energy Dissipation in Monolayer MoS2 Electronics. *Nano Lett.* **2017,** *17* (6), 3429-3433.
(60) Choi, S.; Agafonov, V. N.; Davydov, V. A.; Plakhotnik, T., Ultrasensitive All-Optical Thermometry Using Nanodiamonds with a High Concentration of Silicon-Vacancy Centers and Multiparametric Data Analysis. *ACS Photonics* **2019,** *6* (6), 1387-1392.
(61) Ekimov, E. A.; Kondrin, M. V., Vacancy–impurity centers in diamond: prospects for synthesis and applications. *Physics-Uspekhi* **2017,** *60* (6), 539-558.
(62) Mag-isa, A. E.; Kim, J.-H.; Lee, H.-J.; Oh, C.-S., A systematic exfoliation technique for isolating large and pristine samples of 2D materials. *2D Materials* **2015,** *2* (3), 034017.

For Table of Contents Use Only

Real-time ratiometric optical nanoscale thermometry

Yongliang Chen, Chi Li, Tieshan Yang, Evgeny A. Ekimov, Carlo Bradac, Son Tung Ha, Milos Toth, Igor Aharonovich and Toan Trong Tran[*]

The table of contents describes a nanothermometer based on a single wavelength excitation scheme that enables the real-time collection of the emission intensity ratio of the germanium-vacancy and silicon-vacancy in nanodiamonds which is strongly temperature-dependent.